



## Structural descriptor and surrogate modeling for design of biodegradable scaffolds

Jesse M. Sestito<sup>a,\*</sup>, Tequila A.L. Harris<sup>b</sup>, Yan Wang<sup>b</sup>

<sup>a</sup> College of Engineering, Valparaiso University, Valparaiso, IN, 46383, USA

<sup>b</sup> George W. Woodruff School of Mechanical Engineering, Georgia Institute of Technology, Atlanta, GA, 30332, USA

### ARTICLE INFO

**Keywords:**

Structure-property relationship  
Structural descriptor  
Biodegradable scaffold  
Kinetic Monte Carlo  
Regenerative medicine

### ABSTRACT

Biodegradable scaffolds are important to regenerative medicine in that they provide an amicable environment for tissue regrowth. However, establishing structure-property (SP) relationships for scaffold design is challenging due to the complexity of the three-dimensional porous scaffold geometry. The complexity requires high-dimensional geometric descriptors. The training of such a SP surrogate model will need a large amount of experimental or simulation data. In this work, a schema of constructing SP relationships surrogates is developed to predict the degraded mechanical properties from the initial scaffold geometry. A new structure descriptor, the extended surfacelet transform (EST), is proposed to capture important details of pores associated with the degradation of scaffolds. The efficiency is further enhanced with principal component analysis to reduce the high-dimensional EST data into a low-dimensional representation. The schema also includes a kinetic Monte Carlo biodegradation model to simulate the biodegradation of polymer scaffolds and to generate the training data for the formation of SP relationships. The schema is demonstrated with the design of polycaprolactone biodegradable scaffolds by connecting the initial scaffold geometry to the degraded compressive modulus.

### 1. Introduction

Regenerative medicine is a field in medical sciences that focuses on the regrowth of tissue in human body. This is accomplished primarily through the use of scaffolding. Biodegradable scaffolds have become of increased interest because of their customizability through additive manufacturing and elimination of a post op surgery (Green and Hollister, 2016; Bose et al., 2013). The biodegradation process needs to be well understood in order to design high-quality scaffolds that both support tissue regrowth and meet the target lifecycle. Hydrolysis reactions and water diffusion drive the biodegradation process (Cheung et al., 2007; Mao et al., 2015; von Burkersroda et al., 2002; Lam et al., 2009). The hydrolysis reaction is affected by the scaffold material (Cheung et al., 2007; Mao et al., 2015; Roh et al., 2008), molecular weight (Sevim and Pan, 2018; Wang et al., 2010), scaffold geometry (Heljak et al., 2014a), as well as surface roughness and porosity as a result of manufacturing processes. When modeling the biodegradation process, the geometry of the scaffold strongly influences the degraded mechanical properties (Serra et al., 2013) and biodegradation characteristics (Heljak et al., 2014a). Hence, scaffold geometry is an important aspect of the scaffold design that must be analyzed. Research has been conducted to

understand the impacts of geometry on the scaffold in physiological conditions (Zadpoor, 2015; Scaglione et al., 2014; Porter et al., 2000). However, testing each of these geometries and configurations by either *in vitro* or *in vivo* experiments can be time-consuming and expensive. Current kMC models of scaffold degradation focus on the biodegradation reaction (Mohammadi and Jabbari, 2006; Han and Pan, 2011; Zhang et al., 2017) without emphasis on the impact that the initial scaffold geometry can have on the final degraded properties. As such, it is important to establish an SP linkage between the scaffold geometry and the final degraded properties.

Various physical models regarding the biodegradation of a structure have been developed, such as the hydrolysis reaction (Zhang et al., 2017; Han et al., 2008; Joshi and Mebel, 2007; Entrialgo-Castaño et al., 2008; Chen et al., 2011; Siepmann, 2000), diffusion process (Sevim and Pan, 2018; Zhang et al., 2017; Entrialgo-Castaño et al., 2008; Siepmann, 2000; Soares and Zunino, 2010; Siepmann et al., 2002; Hofmann et al., 2009), and mechanical property degradation (Samami and Pan, 2016; Sharma et al., 2017; Adachi et al., 2006; Heljak et al., 2014b). The overall biodegradation process of the scaffold (Sevim and Pan, 2018; Mohammadi and Jabbari, 2006; Han and Pan, 2011; Zhang et al., 2017; Siepmann et al., 2002; Coffel et al., 2016), has also been extensively

\* Corresponding author. 1900 Chapel Drive, Valparaiso, IN, 46383, USA.

E-mail address: [jesse.sestito@valpo.edu](mailto:jesse.sestito@valpo.edu) (J.M. Sestito).

researched. The latter has been performed using kinetic Monte Carlo (kMC) models, which are an event-driven statistical modeling method. Current kMC models of scaffold degradation focus on the biodegradation reaction (Mohammadi and Jabbari, 2006; Han and Pan, 2011; Zhang et al., 2017) without emphasis on the impact that the initial scaffold geometry can have on the final degraded properties. It is important to establish a SP linkage between the scaffold geometry and the final degraded properties.

Establishing structure-property (SP) relationships is usually done through data-driven methods, such as linear regression model (Ancerewicz et al., 1998; Dai et al., 2020), Gaussian process (GP) model (Zhou et al., 2017; Tran et al., 2018, 2019; Fernandez-Zelaia et al., 2018), and machine learning methods (Li et al., 2021; Baskaran et al., 2020; Griffiths and Harris, 2022). Due to the complexity of the three-dimensional (3D) porous structures in scaffolds (Jones et al., 2007), training the data-driven surrogates of SP relationships requires an efficient description or characterization of the geometry with necessary dimensionality reduction so that the curse of dimensionality can be alleviated. Generic shape descriptors, such as shape matching (Biasotti et al., 2006) and two-point statistics (Kalidindi et al., 2006; Fullwood et al., 2007; Adams et al., 2005), are able to capture binary microstructure information, but more targeted approaches can provide greater insight (Koch et al., 2014; Carleton et al., 2015). To examine porous structures, porosity properties, such as average and extreme pore characteristics (Claes et al., 2016; Bartoš et al., 2018) and pore shapes (Bartoš et al., 2018; Blott and Pye, 2008), provide a targeted approach. A gliding box algorithm has also been applied to examine scaffold geometry to capture more in-depth porosity information than previous methods (Massai et al., 2014). However, the oversimplification of these methods eliminates valuable spatial distribution information of structures. None of the methods were optimized for scaffolds where the salient features of irregular pores need to be captured. Recently Wang et al. (Wang and Rosen, 2010; Huang et al., 2014, 2016) developed a surfacelet transform approach to quantify complex geometries through representative interphase surface features. Interface geometries can be described with surfacelet coefficients after the transformation which emphasizes interphase morphologies. However, the original surfacelets only quantify boundary surface information in the interphase regions. Some SP relationships involved with reactions and diffusions may also be sensitive to the volumes of different phases.

In this work, the surfacelet transform is extended to quantify volumetric information of phases and applied to examine porous scaffolds. Unlike the surfacelet transformation, this method allows for volumetric features of pores, upon which the mechanical and transport properties of scaffolds sensitively depend, to be extracted and directly used in the SP relationships. The extended surfacelet transform (EST) developed in this work captures geometric information of the scaffolds. To further reduce the dimension of the structure descriptor with surfacelet coefficients, principal component analysis (PCA) (Montes de Oca Zapain et al., 2018; Paulson et al., 2018, 2019) is used. PCA is an effective way to create a small set of inputs for a surrogate to form the SP relationship. A new kMC model is built to perform the simulation of hydrolysis reactions in degradation. The compressive modulus of the degraded structure is then predicted with finite element analysis (FEA). The FEA and kMC models are validated. A GP model and linear-regression model of the SP

relationship between the structure descriptor and the modulus of elasticity of the degraded scaffold are constructed.

## 2. Methods

The proposed simulation-based framework to establish the SP relationship for scaffold degradation is shown in Fig. 1. First, 3D models of polymeric scaffolds are built. The structure descriptors of the porous scaffolds are extracted with the EST operation. The biodegradation process with hydrolysis reactions is simulated with kMC. The compressive modulus of elasticity of the degraded polymeric scaffolds is estimated by finite element analysis (FEA). PCA is applied to the surfacelet coefficients to reduce the dimensionality of data. Finally, a GP surrogate model to connect the principal components to the compressive moduli of the degraded scaffolds is developed.

### 2.1. Structure description

Scaffold structures can be modeled in different ways. Voxel representation is used here, where phase information is stored as 3D arrays with values categorized as either void or solid. Voids have the molecular weight (Mn) of zero, whereas the Mn of the solids has different discrete values and represented as positive integers. In experiments, scaffolds are usually fabricated with struts of several 100 μm thick (Lam et al., 2008, 2009; Hollister, 2005; Lu et al., 2012; Gercek et al., 2008). To capture the details of the struts and to keep the computational time low, each voxel is designated as 50 μm x 50 μm x 50 μm. This voxel size allows for several voxels to represent the width of the struts, which requires a reasonable amount of computational time during the kMC and FEA simulations.

To build reliable surrogates of SP relationships, a large amount of training data is needed. The scaffold models can be generated by Monte Carlo sampling. First, a 3D array of the desired cell size is initialized with all void voxels. Next, a specified number of cylinders of random radii and infinite height are generated and placed at a random orientation and position inside the simulation cell. These cylinders are represented by solid voxels. A Mn value is assigned initially to each solid voxel.

Care must be taken to select the inputs of SP surrogates that accurately capture not only the geometry of the scaffold but also the features that are sensitively correlated to the properties. In scaffolds, pore shape and size distributions can be more important to establishing reliable SP linkages to predict material properties than pure solid voxel information. Descriptors need to focus on these geometric features that directly influence material properties. The EST operation is developed to extract the important information of pore sizes and locations.

#### 2.1.1. Extended surfacelet transform

Surfacelet transform was developed to capture 3D boundary distribution information efficiently (Huang et al., 2014, 2016; Duan et al., 2010). EST is an extension of surfacelet transform to capture volume information. For any position  $(x, y, z)$  in the Euclidean space, the volumetric descriptor of a spherical surfacelet is defined as

$$\psi_{x_0, y_0, z_0, r}(x, y, z) = u(r^2 - (x - x_0)^2 - (y - y_0)^2 - (z - z_0)^2) \quad (1)$$

where  $x_0, y_0, z_0$  specify the center of the sphere,  $r$  is an isoparameter that

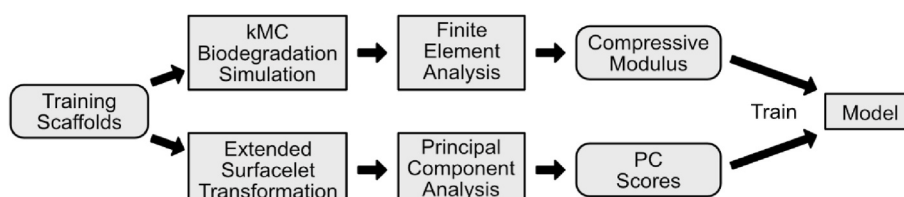


**Fig. 1.** Outline of the training process for the Structure-Property relationship surrogate model.

defines the radius of the sphere, and  $u(\bullet)$  is a step function defined by

$$u(t) = \begin{cases} 0, & (t < 0) \\ 1, & (t \geq 0) \end{cases} \quad (2)$$

The volumetric descriptors of other surfacelets with different shapes can be defined similarly. The EST coefficients of the spherical surfacelet with respect to a property of interest  $f(x, y, z)$  are calculated as

$$\Gamma_f(x, y, z, r) = \int_{-\infty}^{\infty} \int_{-\infty}^{\infty} \int_{-\infty}^{\infty} f(s_1, s_2, s_3) \psi_{x,y,z,r}(s_1, s_2, s_3) ds_1 ds_2 ds_3 \quad (3)$$

$f(x, y, z)$  is defined as a function or field of property. For example, in this work  $f(x, y, z)$  returns the specific molecular weight at location  $x, y, z$  in the scaffold. Similarly, the modulus of elasticity can be used as the function. The EST process is illustrated in Fig. 2 with a 2D case, where the 3D EST coefficients capture the density of  $f_i$  in 2D space with the circular descriptor. For a 3D distribution, the spherical volumetric descriptor results in the 4D EST coefficients, which are dependent on the position  $(x, y, z)$  and radius  $r$  of the sphere.

In a discretized simulation space,  $x, y, z$  correspond to the indices of the discrete voxels. In a domain with  $m \times n \times o$  voxels, the volumetric descriptor is defined as an  $m \times n \times o$  matrix with each element contains the value of  $\psi$  given a specific radius  $r$ . Similarly, the property of interest is defined as a 3D matrix, with 2D slices

$$F[:, :, i] = \begin{bmatrix} f(1, 1, i) & \dots & f(1, n, i) \\ \vdots & \ddots & \vdots \\ f(m, 1, i) & \dots & f(m, n, i) \end{bmatrix} \quad (i = 1, \dots, o) \quad (4)$$

and for a sphere descriptor, this results in the matrix descriptor as

$$\Psi(x, y, z, r)[:, :, i] = \begin{bmatrix} \psi_{x,y,z,r}(1, 1, i) & \dots & \psi_{x,y,z,r}(1, n, i) \\ \vdots & \ddots & \vdots \\ \psi_{x,y,z,r}(m, 1, i) & \dots & \psi_{x,y,z,r}(m, n, i) \end{bmatrix}, \quad (i = 1, \dots, o). \quad (5)$$

The EST coefficient matrix is given as

$$\Gamma_F[x, y, z, r] = \sum_{i,j,k} (F \circ \Psi(x, y, z, r))_{ijk} \quad (6)$$

where  $\circ$  is the Hadamard or element-wise product.

### 2.1.2. Principal component analysis

Though the EST enables the capture of important porous information in the scaffold, this data is high-dimensional, which makes it difficult to be used in constructing surrogates of SP relationships. PCA can be applied to reduce the dimensionality. PCA is an orthogonal linear transformation that allows for the representation of data in a high-dimensional space with principal components (PCs) (Montes de Oca Zapiain et al., 2018; Paulson et al., 2018, 2019). The PCs are sorted as PC

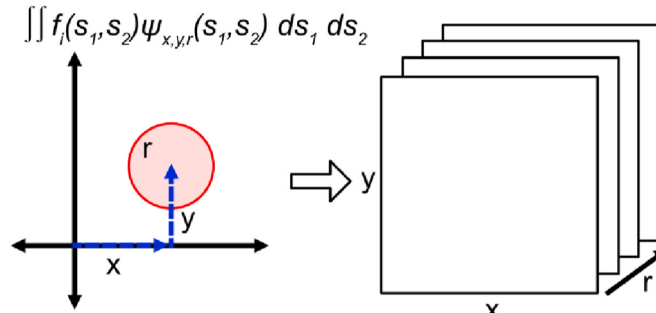


Fig. 2. A two-dimensional illustration of the extended surfacelet transform. In this example, the descriptor is a circular surfacelet. A surface integral is performed to convert two-dimensional  $f_i$  data into three-dimensional data, with the third dimension being the radius of the circular surfacelet.

scores ( $\alpha$ 's) which capture the majority of variance (Var) in the data such that

$$\text{Var}(\alpha_i) \geq \text{Var}(\alpha_j) \quad (1 \leq i < j \leq d). \quad (7)$$

for a total of  $d$  PC scores. PCA prioritizes the most variance in the data by the first few PC scores and the represented variance decreases for each sequential PC score. By selecting the first  $p$  PC scores as the inputs for a surrogate model, the dimension of SP relationships can be reduced.

### 2.1.3. Combining extended surfacelet transform with principal component analysis

To give a brief example on how the EST and PCA can be used in property prediction, let us look at a simple two-dimensional porous structure. A representative volume element (RVE) of a solid homogeneous material with a circular pore is used. As the radius of the pore increases in the 2D RVE, the effective modulus of elasticity decreases. Due to the simplicity of the structure, a point descriptor would be sufficient to capture the important characteristics. A point descriptor with any  $f(x, y)$  would just yield a matrix with  $f(x, y)$  at each  $(x, y)$  point. If more pores were to be added in varying shapes and sizes, a more sophisticated descriptor would be necessary to capture all relevant structural information. PCA can then be used to convert this matrix of numbers into a new domain of PC scores that capture the most important features. In this example, these PC scores would capture pore radius. The relationship between the highest variance PC scores and the final modulus of elasticity can then be established using the PC scores as the independent variables of the surrogate model.

## 2.2. Property prediction

The biodegradation kMC and FEA simulations are developed specifically for polycaprolactone (PCL). This methodology can be modified for other polymers.

Based on the initial structures of scaffolds in voxel representation, kMC simulation is applied to predict the morphological changes in the biodegradation. The mechanical properties of the degraded scaffolds are then estimated from FEA.

### 2.2.1. Biodegradation simulation and hydrolysis rate

kMC can simulate the biodegradation process of a polymeric scaffold by modeling the hydrolysis reactions. The kMC model is developed based on the Stochastic Parallel PARticle Kinetic Simulator (Garcia Cardona et al., 2009) (SPPARKS) to perform the biodegradation simulations. The Mn is defined as

$$\text{Mn} = \frac{\sum_{i=1}^{n_c} M_i}{n_c}. \quad (8)$$

for a number of chains ( $n_c$ ) each of molecular weight ( $M_i$ ). For each voxel, Mn is kept track of, and the hydrolysis reaction events are defined. The reduction of Mn during degradation is treated as single-site events.

The hydrolysis reaction rates are calculated based on the reaction between water ( $H_2O$ ) and ester that produces carboxylic acid (COOH), as



From the first-order kinetics, the change of molarity of COOH functional group can be determined for each voxel from

$$\frac{d[\text{COOH}]}{dt} = k [\text{H}_2\text{O}][\text{ester}] \quad (10)$$

where  $[\bullet]$  is the concentration of a molecule in the voxel and  $k$  is the reaction rate constant. Since each formation of a COOH functional group in the voxel is the result of one polymer scission, the kMC single-site

hydrolysis event rate is calculated as

$$\text{rate} = V \frac{d[\text{COOH}]}{dt}. \quad (11)$$

where  $V$  is the volume of the voxel. The concentrations of water in a void voxel and a solid voxel of 80 kDa PCL are 55.5 molarity (M) and 0.20 M, respectively. The hydrolysis rates obtained from the two cases of void and solid voxels are then used to estimate the rates at the intermediate degradation stages by interpolation.

The hydrolysis rate in Equation (11) only works for homogeneous degradation in a volume. Surface degradation of PCL occurs at a faster rate (Soares and Zunino, 2010). That is, though the PCL scaffold keeps its general shape throughout the degradation process, surface erosion occurs at a faster pace than bulk erosion. The hydrolysis rate of a surface in this work is set to 20% higher than the non-surface structure hydrolysis rate to account for the faster surface erosion. 20% is chosen through visual inspection and qualitative calibration based on the experimental results of Sun et al. (2006) to ensure that surface degradation is captured but not dominant in the degradation process.

The hydrolysis rate calculated from Equation (11) is used for the single-site events in the kMC simulation. The calculation depends on the estimation of the kinetic rate constant  $k$  in Equation (10), which is not used directly in the kMC simulation. The value of  $k$  for PCL can be estimated from the concentration of the main catalyst hydrogen ( $\text{H}^+$ ) (Siparsky et al., 1998), as

$$k = [\text{H}^+] 0.037 \text{ M}^{-2} \text{ day}^{-1}. \quad (12)$$

The concentration of hydrogen in the human body can be determined by the pH level as

$$[\text{H}^+] = 10^{-\text{pH}}. \quad (13)$$

The human body has an average pH level of 7.4.

The initial value for  $k$  obtained from Equation (12) is used to estimate the hydrolysis rate in the initial kMC model. The values of  $k$  and hydrolysis rate are further calibrated by running the kMC simulation and comparing the predicted and experimentally observed degradations. Specifically, the average Mn of the kMC simulation ( $\overline{\text{Mn}}_{\text{kMC}}$ ) is compared to the average Mn of the known degraded state ( $\overline{\text{Mn}}_0$ ) in experiments. The  $k$  value is then adjusted by solving the minimization problem

$$\min_k |\overline{\text{Mn}}_{\text{kMC}} - \overline{\text{Mn}}_0|. \quad (14)$$

The resultant kMC hydrolysis rates gives a final model that gives more accurate predictions of both the trend and magnitude of the biodegradation process.

## 2.2.2. Mechanical property prediction

FEA is used to compute the effective compressive modulus of the degraded scaffolds after kMC simulation. The model is constructed with a collection of cubic cells with each cubic cell corresponding to a voxel. The cubes are assembled to form the overall scaffold. Material properties are assigned to the cubic cells based on their current molecular weights. In this work, it is assumed that the modulus of elasticity for PCL is linearly related to the molecular weight (Adachi et al., 2006) such that 0 kDa implies a modulus of elasticity of 0 MPa and a Mn of 80 kDa corresponds to a modulus of elasticity of 429.1 MPa (Rosa et al., 2004). The Poisson's ratio is assumed to be constant for all levels of Mn (Adachi et al., 2006) and is known to be 0.442 for 65 kDa PCL (Lu et al., 2014). To integrate the kMC biodegradation simulation with FEA, a discretized state from the kMC simulation is used to form the scaffold structure for the FEA model.

The cubes are merged, and of the overall structure, one external face is constrained with zero displacement along two axes and zero rotation

along the two off axes. The opposite external face is imposed with a strain of  $-0.1$  and zero rotation. The scaffold is meshed using tetrahedral elements of size 50  $\mu\text{m}$ . The strain and average stress over time is then used to compute the effective compressive modulus assuming a linear elastic relationship. The FEA simulations are performed in ABAQUS.

## 2.3. Models of SP relationships

A GP surrogate and linear-regression model of the SP relationship are constructed to predict the effective compressive modulus after degradation from the initial geometry described by the first  $p$  significant PC scores ( $\alpha_1, \alpha_2, \dots, \alpha_p$ ). The data necessary to train this model can be obtained utilizing the randomly generated scaffolds, following the procedure shown in Fig. 1. Given a set of samples  $\mathcal{X} = \{x_1, x_2, \dots, x_m\}$  and their known solutions  $f(\mathcal{X}) = \{f(x_1), f(x_2), \dots, f(x_m)\}$ , the surrogate models are trained to predict the expected value of the solution  $f(x_{m+1})$  for a new sample  $x_{m+1}$ .

The GP model is constructed based on the squared-exponential kernel defined as

$$k(x_i, x_j) = s^2 \exp\left(-\frac{d(x_i, x_j)^2}{2l^2}\right) \quad (15)$$

where  $l$  and  $s$  are hyperparameters of scale and  $d(\cdot)$  is the Euclidean distance function (Pedregosa et al., 2011) and the log marginal likelihood is defined by Rasmussen et al. (Rasmussen and Williams, 2006).

Though this work only uses a GP surrogate and linear-regression models, any model, such as splines or nearest neighbors, can be utilized to form the SP relationship.

## 3. Results and discussions

The proposed kMC and FEA models are validated by comparing the calculated effective compressive modulus from the degraded scaffold with experimental results. The SP relationship between the initial scaffold geometry and the effective compressive modulus is then established with a GP model.

### 3.1. Calibration and validation of models

To calibrate the kinetic rate constant  $k$  and the hydrolysis rate, a 2.5 mm long cylinder with 2.5 mm outer diameter and 2.3 mm inner diameter is generated in order to directly compare with the experimental study conducted by Sun et al. (2006). The kMC model is shown in Fig. 3 (a). The periodic boundary condition is applied to the cylinder along its length. 20 different voxels with different levels of Mn are generated with the linear interpolation and equidistance between 66 kDa and 913 Da, where the complete solid voxels are set to 66 kDa. The degradation process of 480 days is simulated in SPPARKS. The *in vivo* experimental results of Sun et al. show that the Mn of PCL drops from the original 66 kDa to about 24 kDa in 480 days (Sun et al., 2006). The rate constant  $k$  is adjusted until the average Mn predicted by the kMC model matches the 24 kDa Mn observed by Sun et al. The resultant degraded structure is shown in Fig. 3 (b).

The calibrated kMC degradation model is used to generate a different scaffold segment, shown in Fig. 4 (a), which was used in the experimental study by Lam et al. (2008). The scaffold is given symmetry along all axes. Similar to the previous case, 20 different voxels are generated with linear interpolation and equidistance between 30 kDa and 913 Da, where the complete solid voxels are set to be 30 kDa of Mn. The degradation of 480 days is simulated in SPPARKS. The degraded scaffold is shown in Fig. 4 (b). The average Mn of the degraded scaffold is 17 kDa.

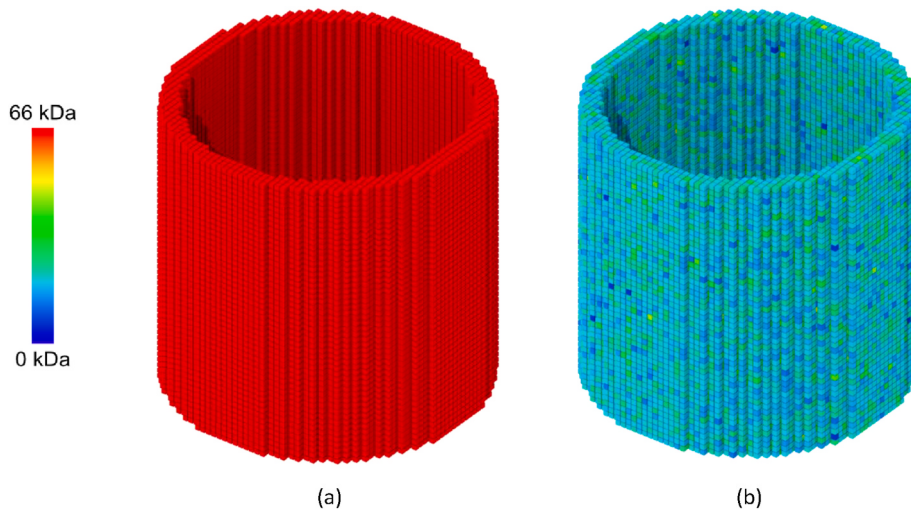


**Fig. 3.** Cylindrical scaffold used for rate calibration in the (a) undegraded and (b) 480 day degraded state. This cylindrical scaffold mirrors that of the experimental study conducted by Sun et al. ([Sun et al., 2006](#)) and is used in the validation of the kMC model.

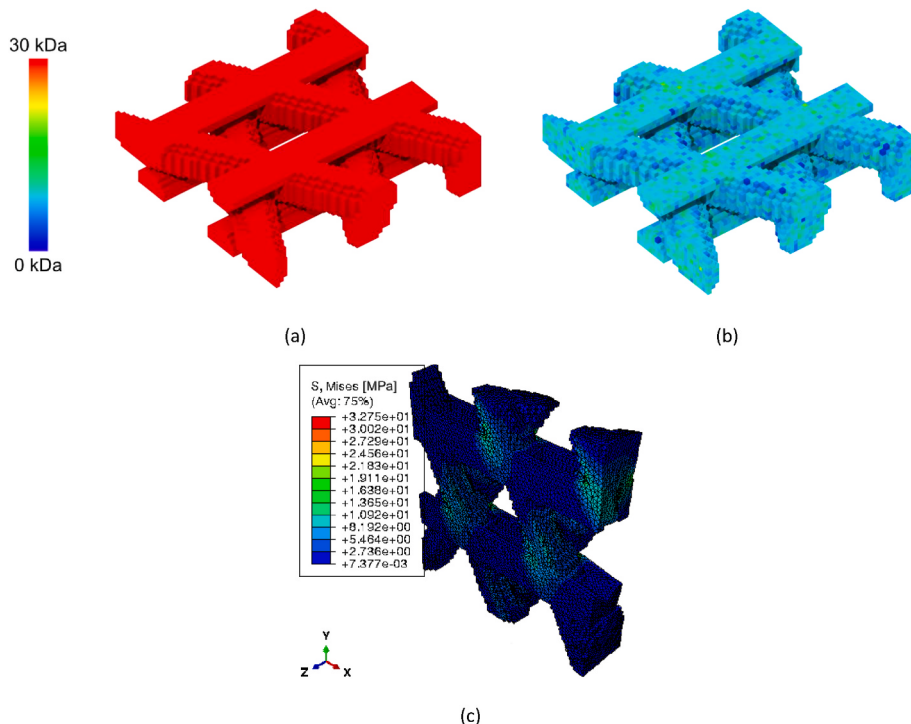


**Fig. 4.** Representative geometry for the validation scaffold in its (a) undegraded state, (b) 480 days degraded state, and (c) compressed state after the finite element analysis simulation. Geometry from Lam et al. used as reference for the representative volume element in (a) ([Lam et al., 2008](#)).

This is in close agreement with the experimental results of 30 kDa as the initial and 16 kDa as the final scaffold ([Lam et al., 2008](#)).

The effective compressive moduli ( $E$ 's) for both the original and degraded scaffolds are computed using FEA, as shown in Fig. 4 (c). The FEA simulations are executed with a 10% compressive strain in the  $y$  direction. The resultant  $E$  values are 47.2 MPa and 29.1 MPa for the original and degraded scaffolds, respectively. A 38% reduction of  $E$  is predicted during the degradation. Experimentally Lam et al. observed that the initial  $E$  of approximately 30 MPa was reduced to 20 MPa when the PCL scaffold is merged and degraded in a phosphate buffered saline solution for 480 days ([Lam et al., 2008](#)). A 33% reduction of  $E$  observed in the experiment is in a close agreement with the kMC and FEA simulations. Overall, the kMC and FEA simulations can predict the

degradation and mechanical properties of scaffolds effectively.

### 3.2. Surrogate construction

To construct the GP surrogate of SP relationship, samples of scaffolds with the size of  $40 \times 40 \times 40$  voxels are generated from some randomly stacked cylinders, where the radii and orientations of the cylinders are sampled from some ranges with uniform distributions. 50 training scaffolds are generated based on each of the five different sets of parameter ranges in Table 1 resulting in a total of 250 models used in constructing the surrogate models. Some examples of the scaffold geometries as shown in Fig. 5. The wide range of scaffold geometries ensure that a reliable SP relationship can be established. This scaffold

**Table 1**

Parameters used to generate the five different randomly generated scaffold groups.

Scaffold Group	Cylinder Radius Range, [Pixels]	Number of Cylinders
A	[3, 5]	15
B	[2, 4]	30
C	[3, 7]	10
D	[12, 17]	4
E	[2, 2]	50

design is similar to that of nanowoven biodegradable scaffolds (Parsons et al., 2022; Kirillova et al., 2021).

The EST with spherical surfacelets is applied to all 250 training scaffolds to generate EST coefficients to describe the geometries. The radius of the surfacelet varies in the sizes of between 1 and 20 voxel widths. For instance, the EST is performed on the 3D scaffold model given in Fig. 5 (a), where a 2D slice at  $z = 20$  is shown in Fig. 6 (a). After the transformation, one slice of the EST coefficients  $\Gamma(x, y, z = 20, r = 3)$  is shown in Fig. 6 (b). For different values of  $r = 8$  and  $r = 15$ , the EST coefficients  $\Gamma(x, y, z = 20, r = 8)$  and  $\Gamma(x, y, z = 20, r = 15)$  are shown in Fig. 6 (c) and Fig. 6 (d) respectively. Larger  $r$  values capture the information about larger pores. In these 2D slices, for  $r = 8$ , the medium-sized pore is most dominant at  $(x, y) = (25, 15)$  where the EST coefficients are the smallest. For  $r = 15$ , the large pore dominates in the center region of the structure. The EST allows for the capture of pore and structure concentration. Having this geometric information improves the surrogate model.

After the kMC simulation of degradation, the effective compressive moduli of all 250 training scaffolds are estimated using FEA. The simulation results are used the outputs to train the GP surrogate and linear-regression models. The inputs are the primary PC scores after PCA is applied to the EST coefficients.

To verify the accuracy of SP relationship, 250 additional verification scaffolds were randomly generated with also 50 scaffolds in each of the five groups. These scaffolds undergo the similar process as in Fig. 1, which allows for the computation of the EST coefficients and the PC

scores from PCA. PC scores capture the variability in the data and can also be used to distinguish between different groups of scaffolds. In Fig. 7 (a), the normalized first and second PC scores calculated from the 250 models of five groups are plotted against each other. It is seen that group D consistently has a higher PC 1 score than the other groups. There is also a distinctive split between group B and group E. Models in group C has slightly larger variability than in other groups. PC 3 and PC 4 are plotted against each other in Fig. 7 (b). Overall, the primary PC scores capture the most important information about the scaffold geometries.

To examine the accuracy of the SP relationship, the compressive modulus predicted from the surrogate  $E_{SP}^{(i)}$  is compared with the one estimated directly from the FEA simulation  $E_{sim}^{(i)}$  for the  $i$ -th verification scaffold. The average error of prediction is calculated by

$$\text{error} = \frac{1}{250} \sum_{i=1}^{250} (E_{sim}^{(i)} - E_{SP}^{(i)}) \quad (16)$$

The error of prediction depends on the type of surrogate model and the number of PC scores used to train the model. This is shown in Fig. 8 (a) for the linear regression model and Fig. 8 (b) for the GP model. There exists a specific number of PC scores that yield a minimum error. This occurs at 10 PC scores and 14 PC scores for the linear regression and GP models respectively. This suggests that as the number of PC scores increases above these optimums, there is overfitting of the training data. It is important to discover the optimal number of PC scores for each type of model. The rest of the analysis is performed with these optimal PC scores. For the linear regression and GP models, the average errors are  $-0.85$  MPa and  $2.44$  MPa, or relatively  $-1.3\%$  and  $3.8\%$ , respectively, as shown in Fig. 8 (c). The linear regression model tends to overestimate the compressive modulus whereas the GP model tends to underestimate. The absolute values of the average errors are  $8.64$  MPa and  $11.90$  MPa for the linear regression model and GP model respectively, with the relative absolute values of  $13.4\%$  and  $18.4\%$  respectively as shown in Fig. 8 (d).

These small error values indicate that a strong SP relationship can be formed between selected descriptors of the initial scaffold geometry and

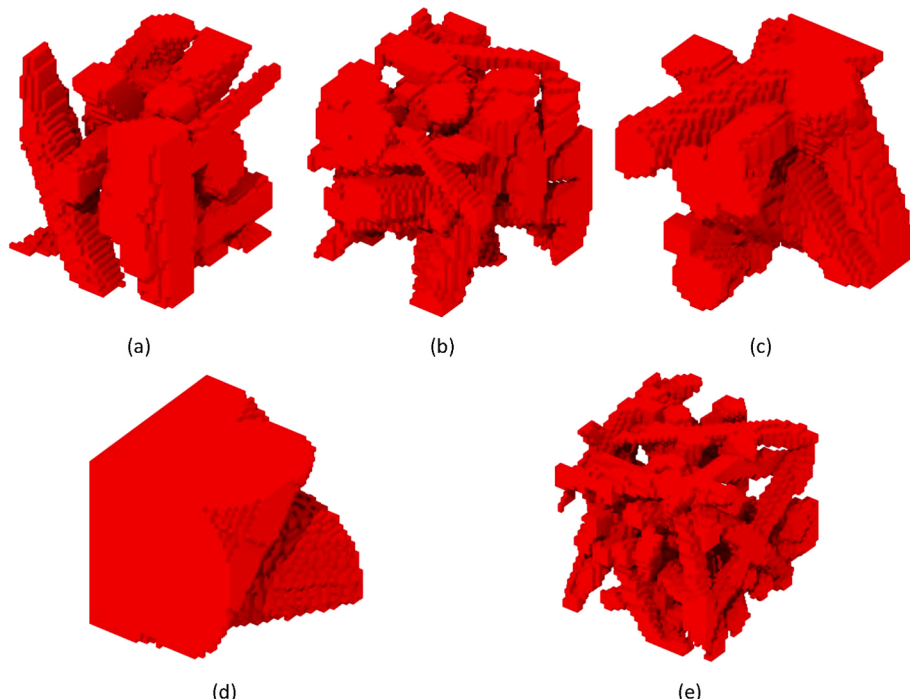


**Fig. 5.** Representative scaffold examples for the five different scaffold groups based on the parameters given in Table 1 where (a) A, (b) B, (c) C, (d) D, and (e) E that have been randomly generated.

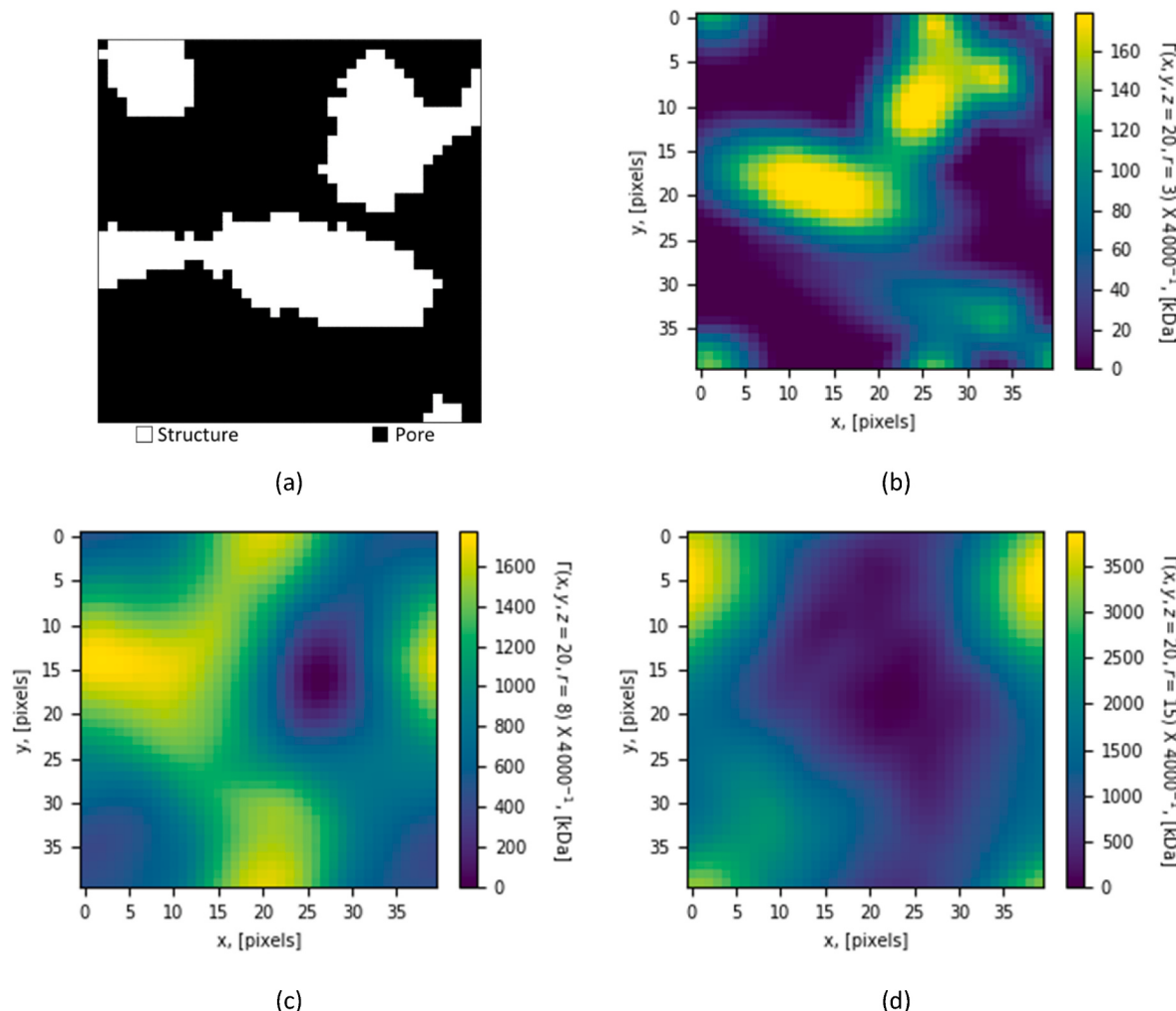


**Fig. 6.** (a) The two-dimensional slice of scaffold at  $z = 20$  for the scaffold in Fig. 5a. The EST is performed using a spherical surfacelet of different radius values (b)  $r = 3$ , (c)  $r = 8$ , and (d)  $r = 15$  pixels. A larger coefficient value corresponds to a higher molecular weight within the spherical region. A lower value corresponds to a lower molecular weight or a larger number of void voxels as pores.

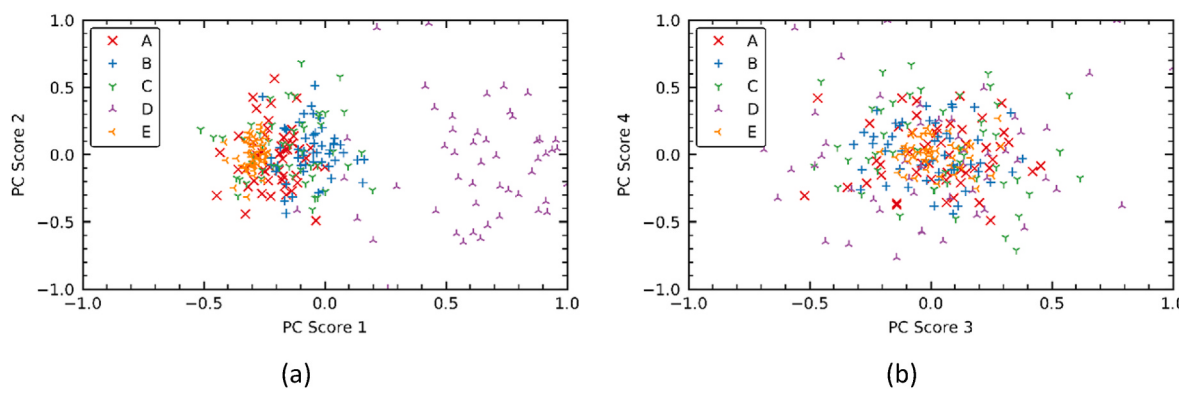


**Fig. 7.** The PC scores (a) 1, 2 and (b) 3, 4 for the 250 verification scaffolds categorized by their identifier.

the mechanical properties of the degraded PCL scaffolds with either model. This SP relationship can be utilized on experimental scaffold geometries, which can be discretized using techniques such as micro-computed tomography ( $\mu$ CT), to provide insight of the final biodegraded compressive modulus prior to expensive *in vitro* and *in vivo* experiments. Using this SP relationship can improve scaffold design and selection.

### 3.3. Limitations

The biodegradation kMC model in this work is a simple model that only incorporates the hydrolysis reaction. To create a more accurate biodegradation model, complex phenomena such as diffusion and crystallization must be incorporated. However, this will greatly increase the overall computation time (Zhang et al., 2017). Care must be made in

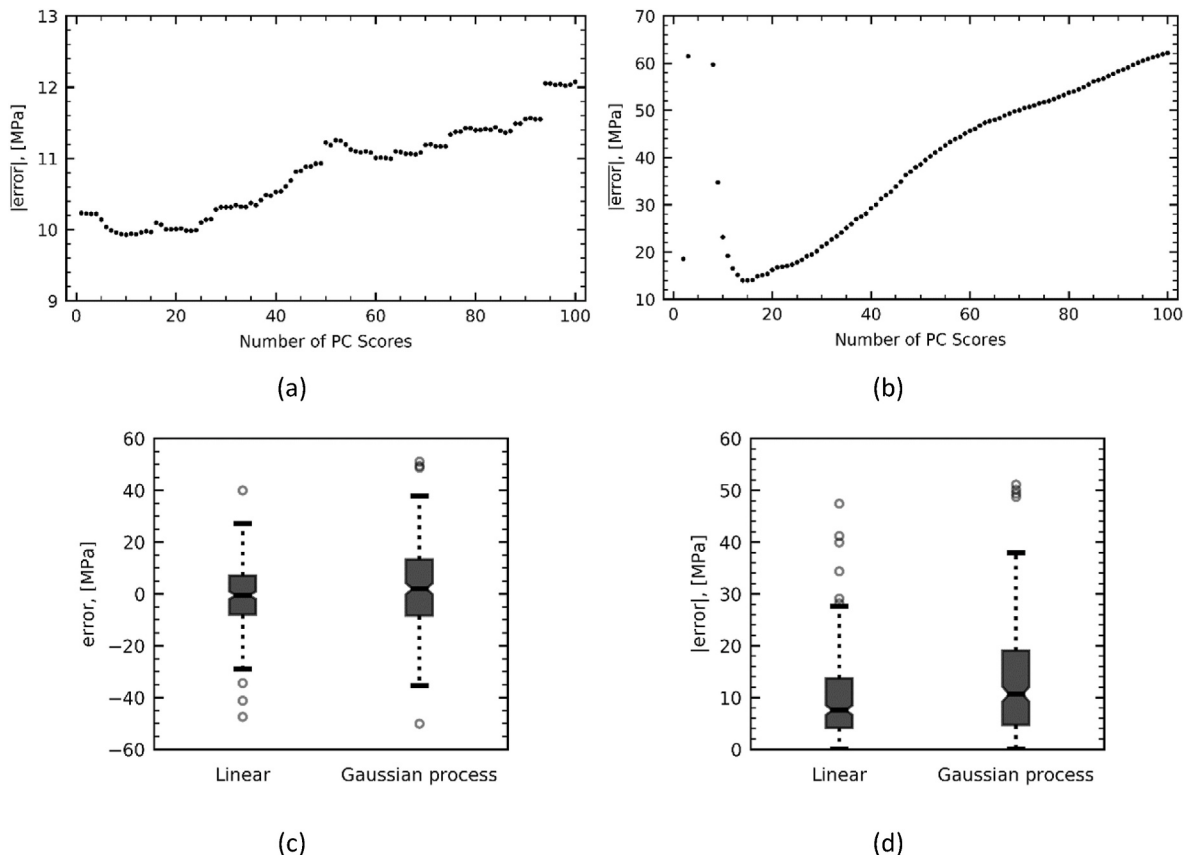


**Fig. 8.** The average error between the verification compressive moduli from the kMC degradation and the predicted compressive moduli calculated from the SP model for the 250 verification scaffolds. The error for an SP model built using a (a) linear model and (b) Gaussian process model plotted against the number of Pareto points used in the model. For the linear model using 10 PC scores and the Gaussian process model using 14 PC scores, the (c) errors and the (d) absolute values of the errors are shown. The circles in (c) and (d) are statistical outliers.

how additional physics is incorporated into the kMC model. In our kMC model, saturated material is assumed to reduce computation time. Though this may be unrealistic, incorporating water diffusion into the kMC model is computationally expensive due to the difference in time scales at which the water diffusion and hydrolysis events occur. Simulating the complex reaction-diffusion processes with kMC remains a research issue.

There are some restrictions to applying the current SP surrogate model. This SP model was created to work for PCL scaffolds of specific types of geometries. Scaffolds with different materials or drastically different types of geometries are likely to have different SP relationships. Additional training data is needed to update the SP surrogates. In addition, the data used to train the SP surrogate are highly dependent on the degradation predicted by the kMC model. Although the kMC model was validated with experimental data, there are inherent approximation and simplification in the event-driven simulation approach. The kMC model can be improved by introducing more events other than the single-site events. This also increases the complexity in calibrating the kMC model with more parameters. Due to the time and cost associated with experimental studies, available experimental data can become insufficient to calibrate the kMC model.

#### 4. Summary and conclusions

In this work, a SP relationship between the initial biodegradable scaffold geometry and the mechanical properties of degraded scaffolds is established. The input parameters of the SP surrogate are the geometric descriptors obtained with the EST and reduced by PCA, and the output is the effective compressive modulus. The newly developed EST is shown

to capture specific volumetric features, such as pores, using spherical descriptors in scaffold geometries. To obtain the effective compressive modulus to train the surrogate, a kMC model is developed to predict the degradation of PCL scaffolds and FEA is used to compute the compressive modulus. 250 training scaffolds were randomly generated to construct a surrogate model. 250 additional scaffolds were generated to verify the accuracy of the surrogate model. Sensitivity studies were conducted and the results show there is an optimum number of PC scores to maximize the accuracy of the SP surrogate depending on the model used. Overall, both the linear and GP surrogates perform well with small prediction errors for the verification scaffolds.

This work shows that a spherical descriptor in the EST can effectively capture geometric information of pores in the scaffolds, which is an important factor in the mechanical properties. The EST can be easily expanded to capture other biodegraded properties, such as transport properties or cell proliferation, or to improve the accuracy of the current property calculations. To do this, new volumetric descriptors need to be used. For example, cylindrical volumes would identify elongated pores and structure while cubic volumes would identify flat surfaces, targeting specific aspects of the scaffold geometry that could be important to the desired properties. By choosing these volumes wisely, the accuracy of the SP relationship can be improved.

In this work, the linear and GP surrogate models perform well. Different surrogate models can be easily incorporated into the proposed method. A new type of model, such as an epoch model or a neural network, or a GP model with a different kernel, could provide more accurate predictions given the periodic nature of the structures.

## CRediT authorship contribution statement

**Jesse M. Sestito:** Conceptualization; Methodology; Investigation; Software; Formal analysis; Visualization; Writing - original draft; Writing - review & editing. **Tequila A. L. Harris:** Conceptualization; Methodology; Writing - original draft; Writing - review & editing; Supervision, **Yan Wang:** Conceptualization; Methodology; Writing - original draft; Writing - review & editing; Funding acquisition; Supervision; Project administration.

## Declaration of competing interest

The authors declare that they have no known competing financial interests or personal relationships that could have appeared to influence the work reported in this paper.

## Data availability

Data will be made available on request.

## Acknowledgements

This work was supported in part by the National Science Foundation through grant CMMI-1663227, as well as the research cyberinfrastructure resources and services provided by the Partnership for an Advanced Computing Environment (PACE) at the Georgia Institute of Technology.

## References

- Adachi, T., Osako, Y., Tanaka, M., Hojo, M., Hollister, S.J., 2006. Framework for optimal design of porous scaffold microstructure by computational simulation of bone regeneration. *Biomaterials* 27, 3964–3972. <https://doi.org/10.1016/j.biomaterials.2006.02.039>.
- Adams, B.L., Gao, X., Kalidindi, S.R., 2005. Finite approximations to the second-order properties closure in single phase polycrystals. *Acta Mater.* 53, 3563–3577. <https://doi.org/10.1016/j.actamat.2005.03.052>.
- Ancerewicz, J., Migliavacca, E., Carrupt, P.A., Testa, B., Brée, F., Zini, R., Tillement, J.P., Labidalle, S., Guyot, D., Chauvet-Monges, A.M., Crevat, A., Le Ridant, A., 1998. Structure-property relationships of trimetazidine derivatives and model compounds as potential antioxidants. *Free Radic. Biol. Med.* 25, 113–120. [https://doi.org/10.1016/S0891-5849\(98\)00072-0](https://doi.org/10.1016/S0891-5849(98)00072-0).
- Bartoš, M., Suchý, T., Foltán, R., 2018. Note on the use of different approaches to determine the pore sizes of tissue engineering scaffolds: what do we measure? *Biomed. Eng. Online* 17, 1–15. <https://doi.org/10.1186/s12938-018-0543-z>.
- Basakaran, A., Kane, G., Biggs, K., Hull, R., Lewis, D., 2020. Adaptive characterization of microstructure dataset using a two stage machine learning approach. *Comput. Mater. Sci.* 177, 109593 <https://doi.org/10.1016/j.commatsci.2020.109593>.
- Biasotti, S., Marini, S., Spagnuolo, M., Falciadino, B., 2006. Sub-part correspondence by structural descriptors of 3D shapes. *CAD Computer Aided Design* 38, 1002–1019. <https://doi.org/10.1016/j.cad.2006.07.003>.
- Blott, S.J., Pye, K., 2008. Particle shape: a review and new methods of characterization and classification. *Sedimentology* 55, 31–63. <https://doi.org/10.1111/j.1365-3091.2007.00892.x>.
- Bose, S., Vahabzadeh, S., Bandyopadhyay, A., 2013. Bone tissue engineering using 3D printing. *Mater. Today* 16, 496–504. <https://doi.org/10.1016/j.mattod.2013.11.017>.
- Carleton, J.B., D'Amore, A., Feaver, K.R., Rodin, G.J., Sacks, M.S., 2015. Geometric characterization and simulation of planar layered elastomeric fibrous biomaterials. *Acta Biomater.* 12, 93–101. <https://doi.org/10.1016/j.actbio.2014.09.049>.
- Chen, Y., Zhou, S., Li, Q., 2011. Mathematical modeling of degradation for bulk-erosive polymers: applications in tissue engineering scaffolds and drug delivery systems. *Acta Biomater.* 7, 1140–1149. <https://doi.org/10.1016/j.actbio.2010.09.038>.
- Cheung, H.Y., Lau, K.T., Lu, T.P., Hui, D., 2007. A critical review on polymer-based bio-engineered materials for scaffold development. *Compos. B Eng.* 38, 291–300. <https://doi.org/10.1016/j.compositesb.2006.06.014>.
- Claes, S., Soete, J., Cnudde, V., Swennen, R., 2016. A three-dimensional classification for mathematical pore shape description in complex carbonate reservoir rocks. *Math. Geosci.* 48, 619–639. <https://doi.org/10.1007/s11004-016-9636-z>.
- Coffel, J., Gandhi, S., Nuxoll, E., 2016. Unified polymer erosion model for pulsatile drug delivery. *J. Membr. Sci.* 512, 61–72. <https://doi.org/10.1016/j.memsci.2016.03.055>.
- Dai, D., Liu, Q., Hu, R., Wei, X., Ding, G., Xu, B., Xu, T., Zhang, J., Xu, Y., Zhang, H., 2020. Method construction of structure-property relationships from data by machine learning assisted mining for materials design applications. *Mater. Des.* 196, 109194 <https://doi.org/10.1016/j.matdes.2020.109194>.
- Duan, B., Wang, M., Zhou, W.Y., Cheung, W.L., Li, Z.Y., Lu, W.W., 2010. Three-dimensional nanocomposite scaffolds fabricated via selective laser sintering for bone tissue engineering. *Acta Biomater.* 6, 4495–4505. <https://doi.org/10.1016/j.actbio.2010.06.024>.
- Entrialgo-Castaño, M., Salvucci, A.E., Lendlein, A., Hofmann, D., 2008. An atomistic modeling and quantum mechanical approach to the hydrolytic degradation of aliphatic polyesters. *Macromol. Symp.* 269, 47–64. <https://doi.org/10.1002/masy.200850908>.
- Fernandez-Zelaia, P., Roshan Joseph, V., Kalidindi, S.R., Melkote, S.N., 2018. Estimating mechanical properties from spherical indentation using Bayesian approaches. *Mater. Des.* 147, 92–105. <https://doi.org/10.1016/j.matdes.2018.03.037>.
- Fullwood, D.T., Adams, B.L., Kalidindi, S.R., 2007. Generalized Pareto front methods applied to second-order material property closures. *Comput. Mater. Sci.* 38, 788–799. <https://doi.org/10.1016/j.commatsci.2006.05.016>.
- Garcia Cardona, C., Webb, I., Blackburn, Edmund, Wagner, G.J., Tikare, V., Holm, E.A., Plimpton, S.J., Thompson, A.P., Slepoy, A., Zhou, X.W., Battaile, C.C., Chandross, M. E., 2009. Crossing the mesoscale no-mans land via parallel kinetic Monte Carlo. <https://doi.org/10.2172/966942>.
- Gerçek, I., Tiğlı, R.S., Gümusderelioglu, M., 2008. A novel scaffold based on formation and agglomeration of PCL microbeads by freeze-drying. *J. Biomed. Mater. Res.* 86, 1012–1022. <https://doi.org/10.1002/jbm.a.31723>.
- Green, G.E., Hollister, S.J., 2016. Computer-aided designed, 3-dimensionally printed porous tissue bioscaffolds. *Otolaryngol. Head Neck Surg.* 152, 57–62. [https://doi.org/10.1177/0194599814552065.Computer-Aided](https://doi.org/10.1177/0194599814552065).
- Griffiths, P.R., Harris, T.A.L., 2022. Machine learning workflow for microparticle composite thin-film process-structure linkages. *J. Coating Technol. Res.* 19, 83–96. <https://doi.org/10.1007/s11998-021-00512-x>.
- Han, X., Pan, J., 2011. Polymer chain scission, oligomer production and diffusion: a two-scale model for degradation of bioresorbable polyesters. *Acta Biomater.* 7, 538–547. <https://doi.org/10.1016/j.actbio.2010.09.005>.
- Han, X., Ding, L., Wang, Y., Pan, J., Sinka, C., 2008. A phenomenological model for the degradation of biodegradable polymers. *Biomaterials* 29, 3393–3401. <https://doi.org/10.1016/j.biomaterials.2008.04.042>.
- Heljak, M.K., Swieszkowski, W., Kurzydłowski, K.J., 2014a. Modeling of the degradation kinetics of biodegradable scaffolds: the effects of the environmental conditions. *J. Appl. Polym. Sci.* 131, 1–7. <https://doi.org/10.1002/app.40280>.
- Heljak, M.K., Swieszkowski, W., Kurzydłowski, K.J., 2014b. Modeling of the degradation kinetics of biodegradable scaffolds: the effects of the environmental conditions. *J. Appl. Polym. Sci.* 131, 1–7. <https://doi.org/10.1002/app.40280>.
- Hofmann, D., Entrialgo-Castaño, M., Kratz, K., Lendlein, A., 2009. Knowledge-based approach towards hydrolytic degradation of polymer-based biomaterials. *Adv. Mater.* 21, 3237–3245. <https://doi.org/10.1002/adma.200802213>.
- Hollister, S.J., 2005. Porous scaffold design for tissue engineering. *Nat. Mater.* 4, 518–524. <https://doi.org/10.1038/nmat1421>.
- Huang, W., Wang, Y., Rosen, D.W., 2014. Inverse surfacelet transform for image reconstruction with constrained-conjugate gradient methods. *J. Comput. Inf. Sci. Eng.* 14, 1–10. <https://doi.org/10.1115/1.4026376>.
- Huang, W., Wang, Y., Rosen, D.W., 2016. Material feature representation and identification with composite surfacelets. *J. Comput. Des. Eng.* 3, 370–384. <https://doi.org/10.1016/j.jcd.2016.06.005>.
- Jones, J.R., Poologasundarampillai, G., Atwood, R.C., Bernard, D., Lee, P.D., 2007. Non-destructive quantitative 3D analysis for the optimisation of tissue scaffolds. *Biomaterials* 28, 1404–1413. <https://doi.org/10.1016/j.biomaterials.2006.11.014>.
- Joshi, S.S., Mebel, A.M., 2007. Computational modeling of biodegradable blends of starch amylose and poly-propylene carbonate. *Polymer* 48, 3893–3901. <https://doi.org/10.1016/j.polymer.2007.04.059>.
- Kalidindi, S.R., Binci, M., Fullwood, D., Adams, B.L., 2006. Elastic properties closures using second-order homogenization theories: case studies in composites of two isotropic constituents. *Acta Mater.* 54, 3117–3126. <https://doi.org/10.1016/j.actamat.2006.03.005>.
- Kirillova, A., Yeazel, T.R., Asheghali, D., Petersen, S.R., Dort, S., Gall, K., Becker, M.L., 2021. Fabrication of biomedical scaffolds using biodegradable polymers. *Chem. Rev.* 121, 11238–11304. <https://doi.org/10.1021/acs.chemrev.0c01200>.
- Koch, R.G., Tsamis, A., D'Amore, A., Wagner, W.R., Watkins, S.C., Gleason, T.G., Vorp, D.A., 2014. A custom image-based analysis tool for quantifying elastin and collagen micro-architecture in the wall of the human aorta from multi-photon microscopy. *J. Biomech.* 47, 935–943. <https://doi.org/10.1016/j.jbiomech.2014.01.027>.
- Lam, C.X.F., Savalani, M.M., Teoh, S.-H., Hutmacher, D.W., 2008. Dynamics of *in vitro* polymer degradation of polycaprolactone-based scaffolds: accelerated versus simulated physiological conditions. *Biomed. Mater.* 3, 034108 <https://doi.org/10.1088/1748-6041/3/3/034108>.
- Lam, C.X.F., Hutmacher, D.W., Schantz, J.T., Woodruff, M.A., Teoh, S.H., 2009. Evaluation of polycaprolactone scaffold degradation for 6 months *in vitro* and *in vivo*. *J. Biomed. Mater. Res.* 90, 906–919. <https://doi.org/10.1002/jbm.a.32052>.
- Li, J., Xie, B., Fang, Q., Liu, B., Liu, Y., Liaw, P.K., 2021. High-throughput simulation combined machine learning search for optimum elemental composition in medium entropy alloy. *J. Mater. Sci. Technol.* 68, 70–75. <https://doi.org/10.1016/j.jmst.2020.08.008>.
- Lu, L., Zhang, Q., Wootton, D., Chiou, R., Li, D., Lu, B., Lelkes, P., Zhou, J., 2012. Biocompatibility and biodegradation studies of PCL/β-TCP bone tissue scaffold fabricated by structural porogen method. *J. Mater. Sci. Mater. Med.* 23, 2217–2226. <https://doi.org/10.1007/s10856-012-4695-2>.
- Lu, L., Zhang, Q., Wootton, D.M., Chiou, R., Li, D., Lu, B., Lelkes, P.I., Zhou, J., 2014. Mechanical study of polycaprolactone-hydroxyapatite porous scaffolds created by

- porogen-based solid freeform fabrication method. *J. Appl. Biomater. Funct. Mater.* 12, 145–154. <https://doi.org/10.5301/JABFM.5000163>.
- Mao, S., Sun, X., Li, B., Su, D.S., 2015. Rationale of the effects from dopants on C-H bond activation for sp2hybridized nanostructured carbon catalysts. *Nanoscale* 7, 16597–16600. <https://doi.org/10.1039/c5nr05759k>.
- Massai, D., Pennella, F., Gentile, P., Gallo, D., Ciardelli, G., Bignardi, C., Audenino, A., Morbiducci, U., 2014. Image-based three-dimensional analysis to characterize the texture of porous scaffolds. *BioMed Res. Int.* 2014 <https://doi.org/10.1155/2014/161437>.
- Mohammadi, Y., Jabbari, E., 2006. Monte Carlo simulation of degradation of porous poly (lactide) scaffolds, 1 effect of porosity on pH. *Macromol. Theory Simul.* 15, 643–653. <https://doi.org/10.1002/mats.200600036>.
- Montes de Oca Zapiain, D., Popova, E., Abdeljawad, F., Foulk, J.W., Kalidindi, S.R., Lim, H., 2018. Reduced-order microstructure-sensitive models for damage initiation in two-phase composites. *Integr Mater Manuf Innov* 7, 97–115. <https://doi.org/10.1007/s40192-018-0112-0>.
- Parsons, R., Sestito, J.M., Luke, B.S., 2022. Computational Analysis and Optimization of Geometric Parameters for Fibrous Scaffold Design. *ACS Omega*. <https://doi.org/10.1021/acsomega.2c05234>.
- Paulson, N.H., Priddy, M.W., McDowell, D.L., Kalidindi, S.R., 2018. Data-driven reduced-order models for rank-ordering the high cycle fatigue performance of polycrystalline microstructures. *Mater. Des.* 154, 170–183. <https://doi.org/10.1016/j.matdes.2018.05.009>.
- Paulson, N.H., Priddy, M.W., McDowell, D.L., Kalidindi, S.R., 2019. Reduced-order microstructure-sensitive protocols to rank-order the transition fatigue resistance of polycrystalline microstructures. *Int. J. Fatig.* 119, 1–10. <https://doi.org/10.1016/j.ijfatigue.2018.09.011>.
- Pedregosa, F., Varoquaux, G., Gramfort, A., Michel, V., Thirion, B., Grisel, O., Blondel, M., Prettenhofer, P., Weiss, R., Dubourg, V., Vanderplas, J., Passos, A., Cournapeau, D., Brucher, M., Perrot, M., Duchesnay, É., 2011. Scikit-learn: machine learning in Python. *J. Mach. Learn. Res.* 12, 2825–2830. <http://jmlr.org/papers/v12/pedregosa11a.html>.
- Porter, B.D., Oldham, J.B., He, S.L., Zobitz, M.E., Payne, R.G., An, K.N., Currier, B.L., Mikos, A.G., Yaszemski, M.J., 2000. Mechanical properties of a biodegradable bone regeneration scaffold. *J. Biomech. Eng.* 122, 286–288. <https://doi.org/10.1115/1.429659>.
- Rasmussen, C.E., Williams, C.K.I., 2006. Gaussian Processes for Machine Learning.
- Roh, J.D., Nelson, G.N., Brennan, M.P., Mirenky, T.L., Yi, T., Hazlett, T.F., Tellides, G., Sinusas, A.J., Pober, J.S., Saltzman, W.M., Kyriakides, T.R., Breuer, C.K., 2008. Small-diameter biodegradable scaffolds for functional vascular tissue engineering in the mouse model. *Biomaterials* 29, 1454–1463. <https://doi.org/10.1016/j.biomaterials.2007.11.041>.
- Rosa, D.S., Neto, I.C., Calil, M.R., Pedroso, A.G., Fonseca, C.P., Neves, S., 2004. Evaluation of the thermal and mechanical properties of and their blends. *J. Appl. Polym. Sci.* 91, 3909–3914.
- Samami, H., Pan, J., 2016. A constitutive law for degrading bioresorbable polymers. *J. Mech. Behav. Biomed. Mater.* 59, 430–445. <https://doi.org/10.1016/j.jmbbm.2016.02.026>.
- Scaglione, S., Ceseracciu, L., Aiello, M., Coluccino, L., Ferrazzo, F., Giannoni, P., Quarto, R., 2014. A novel scaffold geometry for chondral applications: theoretical model and in vivo validation. *Biotechnol. Bioeng.* 111, 2107–2119. <https://doi.org/10.1002/bit.25255>.
- Serra, T., Planell, J.A., Navarro, M., 2013. High-resolution PLA-based composite scaffolds via 3-D printing technology. *Acta Biomater.* 9, 5521–5530. <https://doi.org/10.1016/j.actbio.2012.10.041>.
- Sevim, K., Pan, J., 2018. A model for hydrolytic degradation and erosion of biodegradable polymers. *Acta Biomater.* 66, 192–199. <https://doi.org/10.1016/j.actbio.2017.11.023>.
- Sharma, A., Molla, M.S., Katti, K.S., Katti, D.R., 2017. Multiscale models of degradation and healing of bone tissue engineering nanocomposite scaffolds. *J Nanomech Micromech* 7, 04017015. [https://doi.org/10.1061/\(asce\)nm.2153-5477.0000133](https://doi.org/10.1061/(asce)nm.2153-5477.0000133).
- Siepmann, A.G.J., 2000. Mathematical modeling of bioerodible, polymeric drug delivery systems. *Adv. Drug Deliv. Rev.* 48, 229–247. <https://doi.org/10.1080/01430750.2017.1324812>.
- Siepmann, J., Faisant, N., Benoit, J., 2002. A new mathematical model quantifying drug release from bioerodible microparticles using Monte Carlo simulations. *Pharm. Res. (N. Y.)* 19, 1885–1893. <https://doi.org/10.1023/A:1021457911533>.
- Siparsky, G.L., Voorhees, K.J., Fudu, M., 1998. Hydrolysis of polylactic acid (PLA) and polycaprolactone (PCL) in aqueous acetonitrile solutions: autocatalysis. *J. Environ. Polym. Degrad.* 6, 31–41, 1064–7546/98/0100-0031.
- Soares, J.S., Zunino, P., 2010. A mixture model for water uptake, degradation, erosion and drug release from polydisperse polymeric networks. *Biomaterials* 31, 3032–3042. <https://doi.org/10.1016/j.biomat.2010.01.008>.
- Sun, H., Mei, L., Song, C., Cui, X., Wang, P., 2006. The in vivo degradation, absorption and excretion of PCL-based implant. *Biomaterials* 27, 1735–1740. <https://doi.org/10.1016/j.biomat.2005.09.019>.
- Tran, A., He, L., Wang, Y., 2018. An efficient first-principles saddle point searching method based on distributed kriging metamodels. *ASCE-ASME J. Risk Uncertain Eng. Syst. Part B Mech. Eng.* 4, 1–8. <https://doi.org/10.1115/1.4037459>.
- Tran, A., Furlan, J.M., Pagalthivarthi, K.V., Visintainer, R.J., Wildey, T., Wang, Y., 2019. WearGP: a computationally efficient machine learning framework for local erosive wear predictions via nodal Gaussian processes. *Wear* 422–423. <https://doi.org/10.1016/j.wear.2018.12.081>, 9–26.
- von Burkersroda, F., Schedl, L., Gopferich, A., 2002. Why degradable polymers undergo surface erosion or bulk erosion 23, 4221–4231. [https://doi.org/10.1016/S0142-9612\(02\)00170-9](https://doi.org/10.1016/S0142-9612(02)00170-9).
- Wang, Y., Y., Rosen, D.W., 2010. Multiscale heterogeneous modeling with surfacelets. *Comput Aided Des Appl* 7, 759–776. <https://doi.org/10.3722/cadaps.2010.759-776>.
- Wang, Y., Han, X., Pan, J., Sinka, C., 2010. An entropy spring model for the Young's modulus change of biodegradable polymers during biodegradation. *J. Mech. Behav. Biomed. Mater.* 3, 14–21. <https://doi.org/10.1016/j.jmbbm.2009.02.003>.
- Zadpoor, A.A., 2015. Bone tissue regeneration: the role of scaffold geometry. *Biomater. Sci.* 3, 231–245. <https://doi.org/10.1039/c4bm00291a>.
- Zhang, T., Zhou, S., Gao, X., Yang, Z., Sun, L., Zhang, D., 2017. A multi-scale method for modeling degradation of bioresorbable polyesters. *Acta Biomater.* 50, 462–475. <https://doi.org/10.1016/j.actbio.2016.12.046>.
- Zhou, Q., Wang, Y., Choi, S.K., Jiang, P., Shao, X., Hu, J., 2017. A sequential multi-fidelity metamodeling approach for data regression. *Knowl. Base Syst.* 134, 199–212. <https://doi.org/10.1016/j.knosys.2017.07.033>.